Interstitial Oxide Ion Distribution and Transport Mechanism in Aluminum-Doped Neodymium Silicate Apatite Electrolytes

Tao An,[†,▼] Tom Baikie,[‡] Alodia Orera,[§] Ross O. Piltz,[∥] Martin Meven,[⊥] Peter R. Slater,[#] Jun Wei,*[,¶] María L. Sanjuán,[§] and T. J. White*[,†]

[†]Nanyang Technological University, School of Materials Science and Engineering, 50 Nanyang Avenue, Singapore 639798, Singapore

[‡]Energy Research Institute @ NTU (ERI@N), Nanyang Technological University, Singapore 637553, Singapore

[§]ICMA, CSIC-Universidad de Zaragoza, 50009 Zaragoza, Spain

[∥]Bragg Institute, Australian Science and Technology Organisation, Lucas Heights, New South Wales 2234, Australia

[⊥]RWTH Aachen, Institute of Crystallography and Jülich Centre for Neutron Sciences (JCNS) at Heinz Maier-Leibnitz Zentrum (MLZ), Lichtenbergstraße 1, 85747 Garching, Germany

[#]School of Chemistry, University of Birmingham, Edgbaston, Birmingham B15 2TT, United Kingdom

[¶]Singapore Institute of Manufacturing Technology (SIMTech), Agency for Science, Technology and Research (A*STAR), 71 Nanyang Drive, 638075, Singapore

S *Supporting Information*

ABSTRACT: Rare earth silicate apatites are one-dimensional channel structures that show potential as electrolytes for solid oxide fuel cells (SOFC) due to their high ionic conductivity at intermediate temperatures (500−700 °C). This advantageous property can be attributed to the presence of both interstitial oxygen and cation vacancies, that create diffusion paths which computational studies suggest are less tortuous and have lower activation energies for migration than in stoichiometric compounds. In this work, neutron diffraction of $Nd_{(28+x)/3}Al_xSi_{6-x}O_{26}$ ($0 \leq x \leq 1.5$) single crystals identified the locations of oxygen interstitials, and allowed the deduction of a dual-path conduction mechanism that is a natural extension of the single-path sinusoidal channel trajectory arrived at

through computation. This discovery provides the most thorough understanding of the O^{2-} transport mechanism along the channels to date, clarifies the mode of interchannel motion, and presents a complete picture of O^{2-} percolation through apatite. Previously reported crystallographic and conductivity measurements are re-examined in the light of these new findings.
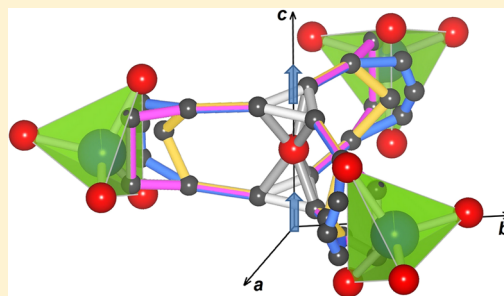
INTRODUCTION

The solid oxide fuel cell (SOFC) is a device that generates electricity from the chemical energy of oxidizable fuels without combustion, leading to much lower and nonpolluting gaseous emissions than that of conventional hydrocarbon-based power production.[1] Compared to other types of high temperature fuel cells, such as the molten carbonate fuel cell (MCFC), the elimination of a liquid phase in the SOFC leads to higher efficiency, greater chemical and physical stability, and provides flexibility in the choice of fuel.[2] Typically, this technology operates at elevated temperatures, which promotes seal failures, necessitates long start-up times, and requires expensive interconnect materials.[3] Ionic conduction in the baseline solid electrolyte, yttria-stabilized zirconia (YSZ), is by vacancy transport and significant above 1000 °C.[4] Therefore, the need exists to discover alternative solid electrolytes that function from 500 to 700 °C. To this end, lanthanoid (*Ln*) silicate/germanate ($Ln_{9.33}(Si/Ge)_6O_{26}$) apatite tunnel structures, through which oxygen can readily migrate, are being examined as intermediate temperature electrolytes.[5]

The structural formula of $Ln_{9.33}Si_6O_{26}$ with $P6_3/m$ symmetry can be expressed as $[Ln^F_{3.33}\square_{0.67}][Ln^T_6][(SiO_4)_6][O_2]$.[6] In terms of descriptive crystallography, rigid SiO_4 tetrahedra are corner-connected to Ln^FO_6 metaprisms that form a framework surrounding the Ln^T atoms, which in turn enclose the tunnel oxygens (Figure 1).[7] To satisfy charge balance, this compound is cation-deficient with the *Ln* vacancies located at the framework site.[8] It has been suggested that these cation vacancies create space for interstitial oxygen,[9] enabling alternative O^{2-} transport paths with lower activation energies.[10] Thus, electrolyte performance is controlled by the cation vacancy and O^{2-} interstitial concentration. For example, in $La_{9.33+x/3}\square_{0.67-x/3}Al_xSi_{6-x}O_{26}$ ($0 \leq x \leq 2$) apatite, the chemical tailoring of Al content ($\square_{La} + 3Si^{4+} \rightarrow La^{3+} + 3Al^{3+}$ most simply) balances steric enhancement due to larger Al expanding the conducting channel against vacancy removal that blocks conduction. Consequently, the highest O^{2-} transport is achieved at the compromise
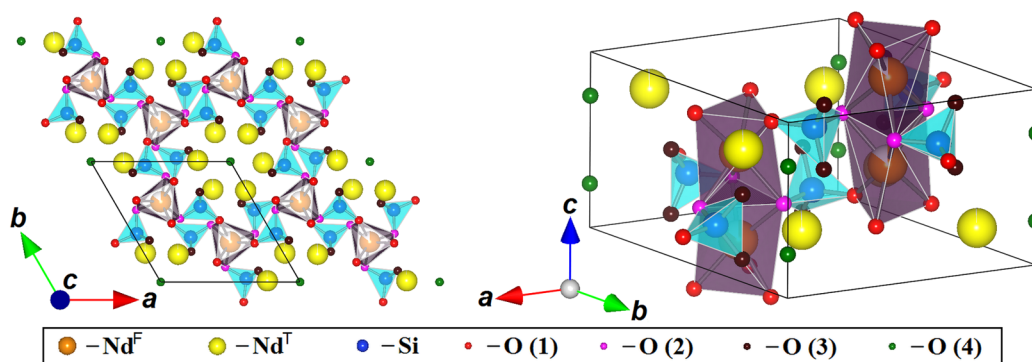
Figure 1. Apatite structure of $Nd_{9.33}Si_6O_{26}$ with $P6_3/m$ symmetry. The Nd(1) (Nd^F) atoms occupy the framework sites ($4f$) and its occupancy is represented by the filled area of the sphere. Each Nd(1) forms a Nd^FO_6 metaprism with three O(1) atoms ($6h$) and three O(2) atoms ($6h$). A framework structure is formed when these metaprisms are corner-connected to SiO_4 tetrahedra (with centered Si ($6h$) bonded to one O(1) ($6h$), one O(2) ($6h$) and two O(3) atoms ($12i$)). This framework surrounds the Nd (2) (Nd^T) atoms ($6h$), which in turn enclose the O (4) atoms ($2a$) located along the c axis tunnel.

composition $x = 1.5$, while fully stoichiometric $La_{10}Al_2Si_4O_{26}$ ($x = 2$) has the lowest conductivity as interstitial transport is denied by the elimination of cation vacancies.[11] As a further example, the oxygen-excess series $La_{9.33+2x/3}Si_6O_{26+x}$ ($0 \leq x \leq 0.5$) has higher conductivity due to extra-stoichiometric interstitial O^{2-}, with maximum mobility achieved for $La_{9.67}Si_6O_{26.5}$ ($x = 0.5$), as La_2SiO_5 appears as a secondary phase for $x > 0.5$ which detracts from overall performance.[12] However, most studies use polycrystalline samples, due to the rarity of large single crystals, and the analysis of intrinsic mobility requires deconvolution from the grain boundary component. Moreover, despite frequent references to "$La_{10}Si_6O_{27}$",[13] the existence of this compound is dubious, as steric restrictions lead to significant M—O (M = La, Si) overbonding. This is in contrast to $La_{10}Ge_6O_{27}$, where lattice expansion ($IR_{Ge} > IR_{Si}$) allows complete filling of interstitial positions.[14]

For $P6_3/m$ lanthanoid silicate apatites, both first-principles simulation[15−18] and neutron diffraction[19] found O^{2-} interstitial migration follows a sinusoidal transport route along the c-axis,[9] passing through saddle points near the SiO_4 tetrahedra at the channel periphery to create pseudo-SiO_5 units, or involves the co-operative displacement of tunnel oxygen.[16,18] In particular, Liao et al. has carried out computational studies of the putative stoichiometric member $La_{10}Al_2Si_4O_{26}$ and suggested an O^{2-} conduction mechanism through migration between AlO_5 and SiO_5 clusters.[20] Simultaneously, conduction of O^{2-} across the ab basal plane is enabled by the presence of interstitials near to, or within, the Ln vacant sites in both silicate[18] and germanate[14] apatites; but such mobility is less significant due to the higher activation energy required.[21,22] Modeling and ^{17}O NMR work have also suggested the importance of exchange processes involving the Si/GeO_4 in this respect.[23]

In our recent study, large single crystals of Al-doped neodymium silicate apatite, $Nd_{(28+x)/3}Al_xSi_{6-x}O_{26}$ ($0 \leq x \leq 1.5$) were successfully grown.[24] The high quality of the material was confirmed by powder X-ray diffraction, electron backscatter diffraction and energy dispersive X-ray spectroscopy, with structural features matched to O^{2-} mobility assessed by AC impedance spectroscopy.[25] The undoped $Nd_{9.33}Si_6O_{26}$ was well described in $P6_3/m$,[26] but the Al-doped crystals showed poorer goodness-of-fit (GOF) due to Nd and O(3) site disorder. Undoped $Nd_{9.33}Si_6O_{26}$ displayed strong anisotropic ionic conductivity, and while the temperature dependent conductivity plot is linear across the ab basal plane, a clear inflection appears in

the c axis conductivity at ∼500 °C. This feature disappeared upon annealing at 950 °C for 3 months and the overall conductivity was lowered. Al-doping increased the conductivity across the ab plane, but mobility was degraded in the c axis direction, to yield an overall improvement for polycrystalline samples.[27]

In this work, neutron diffraction was performed to validate and extend the X-ray study of $Nd_{(28+x)/3}Al_xSi_{6-x}O_{26}$ single crystals with a particular emphasis on recognizing split oxygen positions arising from cation vacancies and discovering low concentrations of interstitial oxygen. Compared to X-ray, the neutron data have shown significant nuclear scattering in these interstitial oxygen positions, and through Fourier mapping,[28] the probability densities (which are time and spatial averages) are measured and from which their respective occupancies could be established. In this way, the structure is studied as a whole dynamic system, instead of focusing onto individual free energy calculations of interstitial oxygen as in first-principles simulation. With the aim of throwing light into the interplay between cation vacancies, oxygen interstitial or split sites and other structural aspects such as long-range symmetry of these apatites, we have measured the Raman spectra of $Nd_{9.33}Si_6O_{26}$ single crystals (both as-grown and annealed) and compared to those of $Nd_8Sr_2Si_6O_{26}$,[29] which serves as reference material due to absence of vacancies and oxygen split sites, and negligible or very low O_{int} content. The availability of single crystals allows quantitative interpretation of spectra, and separates modes with close frequencies, but with different symmetries, that would be indistinguishable in polycrystalline specimens. Ion mobility was inspected over a range of temperatures for the undoped crystal, and the effect of crystallochemical incorporation of aluminum on interstitial abundance and location was correlated with conductivity measurements. From these findings, the conduction paths both along the c axis and across the ab plane were deduced and compared with published simulation mechanisms.

■ EXPERIMENTAL SECTION

Single crystals of $Nd_{(28+x)/3}Al_xSi_{6-x}O_{26}$ ($0 \leq x \leq 1.5$) were grown by the floating zone method as described elsewhere.[24] Preliminary structures were extracted from X-ray diffraction and ionic conductivities measured along the c axis and across the ab plane.[25] Raman measurements were carried out and analyzed in a similar manner as the previous study on $Nd_8Sr_2Si_6O_{26}$ single crystals.[29] Single crystal neutron diffraction was carried out with both the white beam radiation Laue method and a fixed wavelength four-circle method.

Table 1. Refined Atomic Positions and Displacement Parameters of $Nd_{9.33}Si_6O_{26}$ from Fixed Wavelength Diffraction Data Collected at 2 K Using the $P6_3$ Model, which Enables the Specification of the Framework Cation Vacancy Distribution to Be Solely at the 2b Nd(1) Site[a]

atom	Wyckoff	occupancy	x	y	z	U11	U22	U33	U12	U13	U23
Nd(1)	2b	0.75	1/3	2/3	−0.012(1)	0.0038(5)	0.0038(5)	0.0069(7)	0.0019(3)	0	0
Nd(2)	2b	1	2/3	1/3	−0.011(1)	0.0049(4)	0.0049(4)	0.035(1)	0.0024(2)	0	0
Nd(3)	6c	1	0.23032(4)	−0.01049(4)	0.241(1)	0.0056(1)	0.0030(1)	0.0051(1)	0.00220(9)	−0.0005(4)	0.0001(4)
Si	6c	1	0.40121(7)	0.37203(7)	0.241(1)	0.0063(2)	0.0050(2)	0.0048(2)	0.0037(2)	0.0012(8)	−0.0006(7)
O(1)	6c	0.78(1)	0.3268(3)	0.4916(3)	0.243(1)	0.0147(6)	0.0108(6)	0.0077(4)	0.0103(5)	0.0002(7)	−0.0035(7)
O(1)′	6c	0.22(1)	0.2945(9)	0.4581(8)	0.215(1)	0.0147(6)	0.0108(6)	0.0077(4)	0.0103(5)	0.0002(7)	−0.0035(7)
O(2)	6c	1	0.59736(6)	0.47398(6)	0.240(1)	0.0073(2)	0.0069(2)	0.0183(3)	0.0010(2)	0.0001(7)	0.0045(7)
O(3)	6c	0.76(1)	0.3571(6)	0.2576(3)	0.052(1)	0.017(1)	0.0153(8)	0.0049(6)	0.012(1)	−0.0026(8)	−0.0025(6)
O(3)′	6c	0.24(1)	0.308(2)	0.242(1)	0.070(2)	0.017(1)	0.0153(8)	0.0049(6)	0.012(1)	−0.0026(8)	−0.0025(6)
O(4)	6c	0.737(7)	0.3506(4)	0.2529(3)	0.428(1)	0.011(1)	0.0050(6)	0.0068(7)	0.0044(7)	0.0031(7)	0.0016(5)
O(4)′	6c	0.263(7)	0.3012(11)	0.2442(7)	0.402(1)	0.011(1)	0.0050(6)	0.0068(7)	0.0044(7)	0.0031(7)	0.0016(5)
O(5)	2a	0.87(4)	0	0	0.243(1)	0.0074(5)	0.0074(5)	0.035(4)	0.0037(3)	0	0
O(6)	2a	0.16(4)	0	0	0.15(1)	0.026(5)	0.026(5)	0.06(3)	0.013(2)	0	0

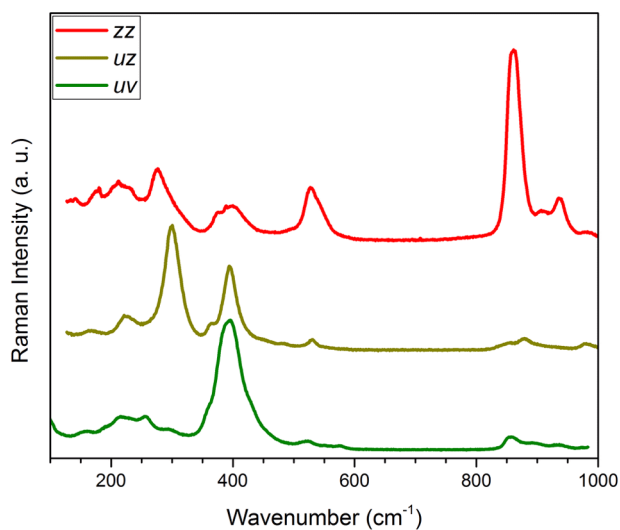[a]This leads to a slightly improved fit (GOF: 1.97, R: 3.07% and Rw: 2.97%) as compared to $P6_3/m$ model.

Table 2. Refined Atomic Positions and Displacement Parameters of $Nd_{9.33}Si_6O_{26}$ from Fixed Wavelength Diffraction Data Collected at 2 K Using the $P6_3/m$ Model[a]

atom	Wyckoff	occupancy	x	y	z	U11	U22	U33	U12	U13	U23
Nd(1)	4f	0.859(4)	1/3	2/3	−0.0009(1)	0.0042(2)	0.0042(2)	0.0201(3)	0.00211(9)	0	0
Nd(2)	6h	1	0.01049(5)	0.24082(5)	1/4	0.0031(2)	0.0043(2)	0.0051(2)	0.0009(1)	0	0
Si	6h	1	0.40128(9)	0.37210(9)	1/4	0.0066(3)	0.0053(3)	0.0048(3)	0.0038(2)	0	0
O(1)	6h	0.70(2)	0.3287(5)	0.4938(5)	1/4	0.0109(9)	0.0067(10)	0.0068(4)	0.0064(9)	0	0
O(1)′	12i	0.139(8)	0.2978(9)	0.4608(9)	0.2282(8)	0.0109(9)	0.0067(10)	0.0068(4)	0.0064(9)	0	0
O(2)	6h	1	0.59729(7)	0.47399(7)	1/4	0.0075(2)	0.0068(2)	0.0176(3)	0.0010(2)	0	0
O(3)	12i	0.753(3)	0.35337(12)	0.25487(8)	0.0618(1)	0.0155(4)	0.0103(2)	0.0058(2)	0.0086(2)	−0.0030(2)	−0.0022(2)
O(3)′	12i	0.247(3)	0.3038(4)	0.2437(3)	0.0851(3)	0.0155(4)	0.0103(2)	0.0058(2)	0.0086(2)	−0.0030(2)	−0.0022(2)
O(4)	2a	0.88(3)	0	0	1/4	0.0075(5)	0.0075(5)	0.037(3)	0.0038(3)	0	0
O(5)	4e	0.08(2)	0	0	0.15(1)	0.036(8)	0.036(8)	0.06(3)	0.018(4)	0	0

[a]The fit is slightly inferior (GOF: 2.37, R: 3.56%, and Rw: 3.47%) as compared to the $P6_3$ model, but for the present crystals best represents the average symmetry.
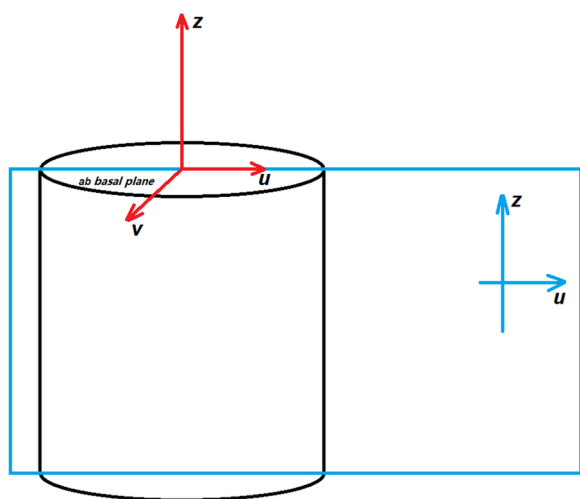
Figure 2. Schematic diagram showing the configurations of the Raman measurements. u and v are two perpendicular directions in the ab basal plane, and u is perpendicular to z, which is along the crystallographic c axis. Under this configuration, the uv, zz, and uz spectra correspond to E_{2g}, A_g, and E_{1g} symmetries, respectively.

Figure 3. Raman spectra of an as-grown $Nd_{9.33}Si_6O_{26}$ single crystal collected at room temperature.

Table 3. Raman Shifts (cm^{-1}) of As-Grown $Nd_{9.33}Si_6O_{26}$ Single Crystal Derived from Profile Fitting of zz, uz, and uv Spectra, Yielding A_g, E_{1g}, and E_{2g} Modes, Respectively

	A_g modes	E_{1g} modes	E_{2g} modes	assignment
	107	96.3	99	lattice and librational modes
	128.4	162.7	113	
	139.3	182.4	161.5	
	172.6	220	192.5	
	206	242	213.4	
	231	264.2	233.8	
	248.5 vw	298	259	
	271.7		293.6	
	286.8 b		329.5	
	317 b			
	371 b	361.8	361.5	ν_2 and other oxygen vibrations
	396.3	392.6	381.4	
	456.8 vb	415	400	
		442 vb	430	
		484	457 vb	
	500 vb	512 vw	492 wb	ν_4 and other oxygen vibrations
	523.6	528.2	524.8	
	539.4	542 vb	555	
			578	
	851.6	842.2	852.4	ν_1 and ν_3
	861.4	854.4	861.1	
	880	874.8	896.2	
	904	895.7	938	
	934.6	930.5	981.3	
	982.5	980		
total:	22	21	23	

Data were collected at 4, 100, 300, 573, and 773 K for the undoped $Nd_{9.33}Si_6O_{26}$ crystal. For the x = 0.5, 1.0, and 1.5, Al-doped $Nd_{(28+x)/3}Al_xSi_{6-x}O_{26}$ data were accumulated at 100 K.

Fixed Wavelength Four-Circle Method. To validate outcomes from the Laue experiments, single crystal neutron diffraction data were also collected from as-grown $Nd_{9.33}Si_6O_{26}$ crystals at 2K and room temperature, and for an annealed $Nd_{9.33}Si_6O_{26}$ crystal (950 °C/3 months) at room temperature on the HEiDi diffractometer at FRM-II (Heißes Einkristalldiffraktometer, hot source, Garching, Germany). A wavelength of 1.17 Å combined with a high flux density of 1.2×10^7 neutrons per second per cm^2 was obtained using an Er filter and a Ge (311) monochromator. Low temperatures were realized by an He closed-cycle cryostat mounted in the Eulerian cradle of the diffractometer. The crystal was wrapped in Al foil to minimize thermal losses, and the temperature measured and controlled by a diode sensor near the heater to a stability of ±0.1K. The absolute temperatures were measured by an additional temperature sensor at the sample. The corrected integrated intensities of the reflections were calculated using PRON2K,[37] and numerical absorption correction was performed with TBAR.[38] Further instrument details can be found in Meven et al.[39−41] Data collected have $(\sin \theta/\lambda)_{max} > 0.72$, and the total number of reflections are >3000. Corrections for the extinction effect[42] were made in the refinements.

Laue Method. Single crystal neutron diffraction data were collected on the KOALA Laue diffractometer at the Open Pool Australian Lightwater (OPAL) reactor operated by the Australian Nuclear Science and Technology Organisation (ANSTO). The Laue method uses polychromatic thermal-neutrons coupled with a large solid-angle (8 steradians) cylindrical image-plate detector. The as-grown apatite crystals of approximate dimensions $1.5 \times 1.5 \times 1.5$ mm^3 were mounted on an aluminum pin with silicone grease. The diffraction patterns were indexed using LAUEGEN[30,31] and the reflections integrated using a 2D version of the $\sigma(I)/I$ algorithm described by Wilkinson et al.[32] and Prince et al.[33] No absorption correction was necessary. The reflections were normalized to the same incident wavelength using a curve derived by comparing equivalent reflections and multiple observations via the program LAUENORM.[34] Only reflections with wavelengths between 1.0 and 2.9 Å were accepted as those outside this range were too weak, or had too few equivalents, to allow determination of the normalization curve confidently. Structures were determined using Jana 2006[35] with the starting model derived from single crystal X-ray diffraction.[25] VESTA[36] was used for 3D visualization of the difference Fourier maps that allow identification of structural disorder and interstitial oxygen.

RESULTS

In previous single crystal X-ray diffraction work, O(3)′ split sites were identified only in undoped as-grown $Nd_{9.33}Si_6O_{26}$ single crystals.[25] Such features, however, were found in both Al-doped $Nd_{(28+x)/3}Al_xSi_{6-x}O_{26}$ (x = 0.5, 1.0 and 1.5) and annealed $Nd_{9.33}Si_6O_{26}$ single crystals in this neutron study. This is mainly due to the fact that a much larger volume was inspected during the neutron diffraction experiment, and neutrons are more sensitive to oxygen positions, while the single crystal X-ray

Table 4. Refined Atomic Parameters from Laue Neutron Diffraction of $P6_3/m$ Nd$_{9.33}$Si$_6$O$_{26}$ as a Function of Temperature

temperature (K)	4	100	300	573	773
GOF	1.95	2.02	1.74	1.99	1.94
R (%)	5.72	6.67	6.55	12.43	12.87
R_w (%)	8.00	4.53	3.86	5.56	5.44
Nd(1), 4f, ($^1/_3$ $^2/_3$ z)					
z	−0.0009(1)	−0.0009(1)	−0.0007(1)	−0.0002(2)	−0.0002(2)
occupancy	0.901(4)	0.895(5)	0.888(5)	0.902(6)	0.892(6)
U_{iso} (Å^2)	0.0098(2)	0.0112(3)	0.0129(2)	0.0180(4)	0.0208(4)
Nd(2), 6h, (x y $^1/_4$)					
x	0.01016(6)	0.01024(7)	0.01026(6)	0.01020(9)	0.01028(9)
y	0.24023(6)	0.24016(7)	0.23985(6)	0.2391(1)	0.2388(1)
U_{iso} (Å^2)	0.0041(2)	0.0053(2)	0.0078(2)	0.0129(3)	0.0162(3)
Si, 6h, (x y $^1/_4$)					
x	0.4014(1)	0.4015(1)	0.4016(1)	0.4015(2)	0.4017(2)
y	0.3723(1)	0.3723(1)	0.3725(1)	0.3727(2)	0.3728(2)
U_{iso} (Å^2)	0.0046(3)	0.0052(3)	0.0068(3)	0.0103(4)	0.0127(4)
O(1), 6h, (x y $^1/_4$)					
x	0.3232(2)	0.3228(1)	0.3231(1)	0.3235(2)	0.3235(2)
y	0.4878(1)	0.4872(1)	0.4873(1)	0.4874(2)	0.4874(2)
U_{iso} (Å^2)	0.0155(3)	0.0167(4)	0.0195(3)	0.0260(6)	0.0305(6)
O(2), 6h, (x y $^1/_4$)					
x	0.59762(9)	0.5974(1)	0.59725(9)	0.5969(2)	0.5966(2)
y	0.4740(1)	0.4738(1)	0.4736(1)	0.4734(2)	0.4731(2)
U_{iso} (Å^2)	0.0115(2)	0.0128(3)	0.0157(2)	0.0223(4)	0.0266(4)
O(3), 12i, (x y z)					
occupancy	0.763(4)	0.763(5)	0.753(5)	0.733(9)	0.734(9)
x	0.3533(2)	0.3532(2)	0.3532(2)	0.3538(4)	0.3537(4)
y	0.2551(1)	0.2552(1)	0.2554(1)	0.2560(2)	0.2564(2)
z	0.0615(1)	0.0616(2)	0.0615(2)	0.0614(3)	0.0617(3)
U_{iso} (Å^2)	0.0096(3)	0.0111(4)	0.0139(4)	0.0198(7)	0.0246(8)
O(3)′, 12i, (x y z)					
occupancy	0.237(4)	0.237(5)	0.247(5)	0.267(9)	0.266(9)
x	0.3044(6)	0.3038(7)	0.3048(6)	0.306(1)	0.304(1)
y	0.2446(4)	0.2446(5)	0.2449(4)	0.2467(8)	0.2463(8)
z	0.0863(4)	0.0863(5)	0.0867(4)	0.0868(8)	0.0880(8)
U_{iso} (Å^2)	0.0096(3)	0.0111(4)	0.0139(4)	0.0198(7)	0.0246(8)
O(4), 2a, (0 0 $^1/_4$)					
occupancy	0.895(9)	0.92(1)	0.89(1)	0.96(1)	0.95(1)
U_{iso} (Å^2)	0.0207(5)	0.0238(7)	0.0281(6)	0.046(1)	0.052(1)

Table 5. Refined Anisotropic Atomic Displacement Parameters (ADP) from Laue Neutron Diffraction of $P6_3/m$ Nd$_{9.33}$Si$_6$O$_{26}$ as a Function of Temperature

temperature (K)	4	100	300	573	773
Nd (1), 4f, (1/32/3z)					
U_{11}	0.0056(3)	0.0073(3)	0.0092(3)	0.0148(4)	0.0187(4)
U_{33}	0.0183(4)	0.0191(4)	0.0205(4)	0.0245(6)	0.0249(6)
Nd (2), 6h, (x y 1/4)					
U_{11}	0.00268(19)	0.0038(2)	0.0063(2)	0.0112(3)	0.0143(3)
U_{22}	0.0041(2)	0.0052(3)	0.0078(2)	0.0128(4)	0.0158(4)
U_{33}	0.0043(2)	0.0055(2)	0.0078(2)	0.0125(3)	0.0160(3)
U_{12}	0.0007(2)	0.0011(2)	0.0024(2)	0.0045(3)	0.0057(3)
Si, 6h, (x y 1/4)					
U_{11}	0.0062(4)	0.0067(4)	0.0080(4)	0.0117(6)	0.0139(6)
U_{22}	0.0049(4)	0.0054(4)	0.0073(4)	0.0106(6)	0.0127(6)
U_{33}	0.0041(3)	0.0047(3)	0.0064(3)	0.0105(4)	0.0131(4)
U_{12}	0.0038(3)	0.0038(3)	0.0049(3)	0.0069(5)	0.0077(5)
O (1), 6h, (x y 1/4)					
U_{11}	0.0242(4)	0.0263(5)	0.0304(5)	0.0395(8)	0.0460(8)
U_{22}	0.0218(4)	0.0232(5)	0.0256(4)	0.0330(7)	0.0379(7)
U_{33}	0.0122(3)	0.0131(3)	0.0158(3)	0.0218(5)	0.0263(5)
U_{12}	0.0203(4)	0.0216(4)	0.0240(4)	0.0303(7)	0.0351(7)

Table 5. continued

| temperature (K)	4	100	300	573	773
O (2), 6h, (x y 1/4)					
U_{11}	0.0076(3)	0.0084(4)	0.0098(3)	0.0135(5)	0.0159(5)
U_{22}	0.0061(3)	0.0074(4)	0.0094(3)	0.0153(5)	0.0190(6)
U_{33}	0.0170(3)	0.0192(3)	0.0234(3)	0.0331(6)	0.0391(6)
U_{12}	0.0006(2)	0.0014(3)	0.0014(3)	0.0035(4)	0.0044(4)
O (3), 12i, (x y z)					
U_{11}	0.0170(6)	0.0196(7)	0.0241(7)	0.033(1)	0.039(1)
U_{22}	0.0108(3)	0.0122(3)	0.0152(3)	0.0217(5)	0.0261(6)
U_{33}	0.0046(3)	0.0057(3)	0.0075(3)	0.0119(5)	0.0156(6)
U_{12}	0.0097(3)	0.0110(4)	0.0136(4)	0.0188(8)	0.0219(8)
U_{13}	−0.0032(3)	−0.0040(4)	−0.0048(3)	−0.0066(7)	−0.0086(7)
U_{23}	−0.0026(2)	−0.0032(2)	−0.0040(2)	−0.0060(4)	−0.0078(4)
O (4), 2a, (0 0 1/4)					
U_{11}	0.0085(6)	0.0110(7)	0.0122(7)	0.020(1)	0.024(1)
U_{33}	0.045(1)	0.049(1)	0.060(1)	0.097(3)	0.109(3)
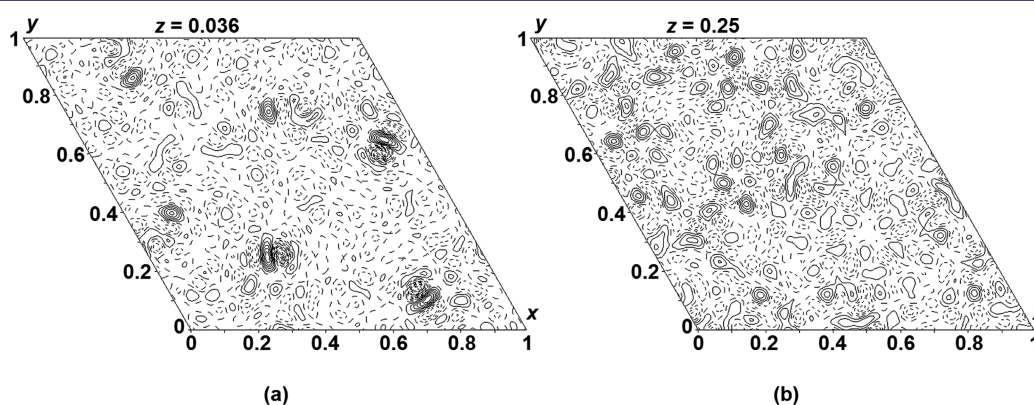
Figure 4. Representative difference Fourier maps obtained from the as-grown $P6_3/m$ $Nd_{9.33}Si_6O_{26}$ crystal with neutron diffraction data collected at (a) 4 K and (b) 773 K. Locations with closely spaced contours reflect the positions of interstitial oxygen. The step size of the positive (solid line) and negative (dotted line) contours is 0.5 fm.

Table 6. Oxygen Interstitial Positions and Peak Concentrations from Laue Neutron Diffraction of $P6_3/m$ $Nd_{9.33}Si_6O_{26}$ as a Function of Temperature, Arranged from Highest to Lowest Concentration[a]

	x	y	z	conc. (Å⁻³)
4 K				
$O_{Int}1$	0.1429	0.3981	0.0361	0.098
$O_{Int}2$	0.0832	0.3085	0.0554	0.084
$O_{Int}3$	0.0003	0.0003	0.1539	0.081
$O_{Int}4$	0.7622	0.0851	0.2163	0.072
100 K				
$O_{Int}1$	0.7302	0.1313	1/4	0.083
$O_{Int}2$	0.1431	0.4042	0.0382	0.076
$O_{Int}3$	0.0002	0.0002	0.1434	0.074
$O_{Int}4$	0.0686	0.4393	0.0279	0.071
$O_{Int}5$	0.3865	0.1276	0.024	0.071
300 K				
$O_{Int}1$	0.1300	0.4034	0.037	0.074
$O_{Int}2$	0.0001	0.0001	0.1304	0.067
$O_{Int}3$	0.5079	0.1627	0.0358	0.045
573 K				
$O_{Int}1$	0.1507	0.3933	0.0354	0.093
$O_{Int}2$	0.6248	0.0643	0.0557	0.088
$O_{Int}3$	0.9891	0.895	0.0596	0.088
$O_{Int}4$	0.0643	0.9214	0.0932	0.084
$O_{Int}5$	0.5911	0.8222	0.0674	0.083
773 K				
$O_{Int}1$	0.5056	0.0271	1/4	0.088
$O_{Int}2$	0.2381	0.406	1/4	0.086

Table 6. continued

	x	y	z	conc. (Å⁻³)
773 K				
$O_{Int}3$	0.3575	0.4281	1/4	0.083
$O_{Int}4$	0.8912	0.0109	0.0360	0.081
$O_{Int}5$	0.4492	0.0246	1/4	0.079
$O_{Int}6$	0.0513	0.4567	1/4	0.078
$O_{Int}7$	0.1348	0.4017	0.0454	0.076
$O_{Int}8$	0.1388	0.3053	1/4	0.076
$O_{Int}9$	0.9406	0.0052	0.0875	0.076

[a]Additional interstitial positions ($O_{int}3$) were detected in the tunnel at 573 K and ($O_{int}1$, $O_{int}5$, $O_{int}6$) between SiO_4 tetrahedra at 773 K.

diffraction data were dominated by the contribution from the heavier Nd element. While the space group for $Nd_{9.33}Si_6O_{26}$ apatite is reportedly $P6_3/m$, based on single crystal X-ray diffraction data,[26] a careful neutron diffraction study on $La_{9.33}Si_6O_{26}$ suggested the true symmetry of this La analogue to be $P6_3$.[43] Therefore, both $P6_3/m$ and $P6_3$ models were tested for the fixed wavelength diffraction data collected at 2 K. In $P6_3$, removal of the mirror plane perpendicular to c axis allows the framework 4f Nd(1) site to split into two 2b sites, Nd(1) and Nd(2), and the 12i O(3) to split into two 6c sites, O(3) and O(4) (Table 1). Introducing this extra degree of freedom at the former sites enables better fitting of the cation vacancies by ensuring no Nd vacancies can occur next to each other, and a slightly improved GOF compared to $P6_3/m$ (Table 2), which, however, did not fundamentally improve the quality of the structure
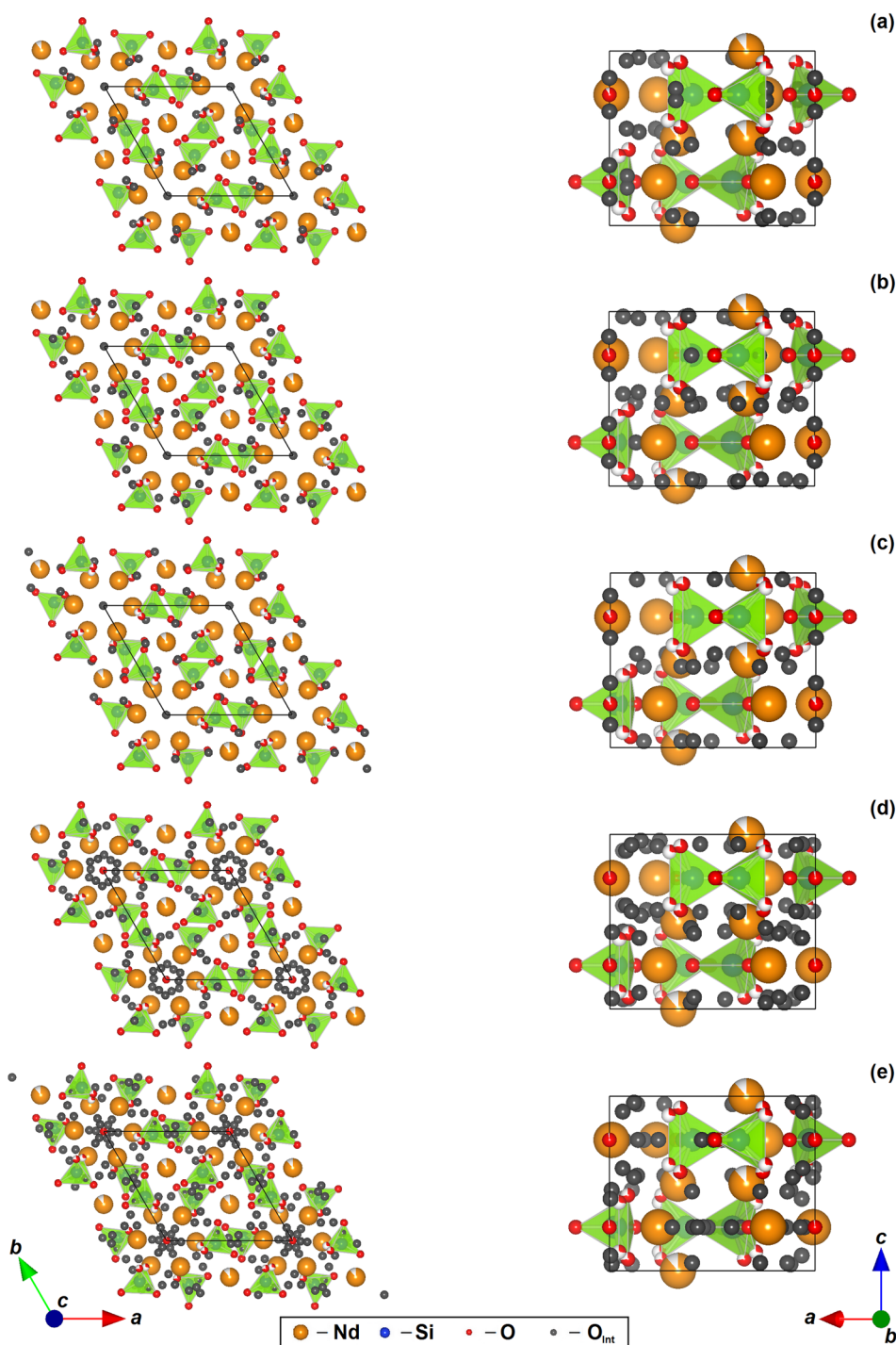
Figure 5. Concentration and distribution of oxygen interstitials in $P6_3/m$ Nd$_{9.33}$Si$_6$O$_{26}$ at (a) 4 K, (b) 100 K, (c) 300 K, (d) 573 K, and (e) 773 K viewed along [001] (left) and [010] (right).

determination. In addition, the error bars of site positions in $P6_3/m$, especially those of z-coordinates, are significantly smaller than those in $P6_3$.

To confirm the space group of Nd$_{9.33}$Si$_6$O$_{26}$, as well as the oxygen site splitting, Raman spectroscopy was carried out on the single crystal samples. The expected Raman activities for $P6_3$ and $P6_3/m$ space symmetries are shown in Tables S1 and S2 (Supporting Information, SI), respectively. The higher activity in $P6_3$ comes from the loss of inversion symmetry. It should be noted that the total number of expected modes in these tables includes internal, librational, and lattice translational modes, and

in compounds with tetrahedral moieties such as [SiO$_4$]$^{4-}$, the main bands are usually attributed to internal vibrations of the tetrahedra. Therefore, comparison between the number and symmetry of internal modes (in both space groups) with experimental results is probably more instructive than the total number of expected modes. The internal modes of tetrahedral anions are denoted as ν_1 (symmetric stretching), ν_2 (symmetric bending), ν_3 (asymmetric stretching), and ν_4 (asymmetric bending). For free [SiO$_4$]$^{4-}$ these modes appear at 819 cm^{-1} (ν_1), 956 cm^{-1} (ν_3), 340 cm^{-1} (ν_2), and 527 cm^{-1} (ν_4),[44] while in rare earth silicate apatites these frequencies may vary (depending

(a)

(b)

(c)
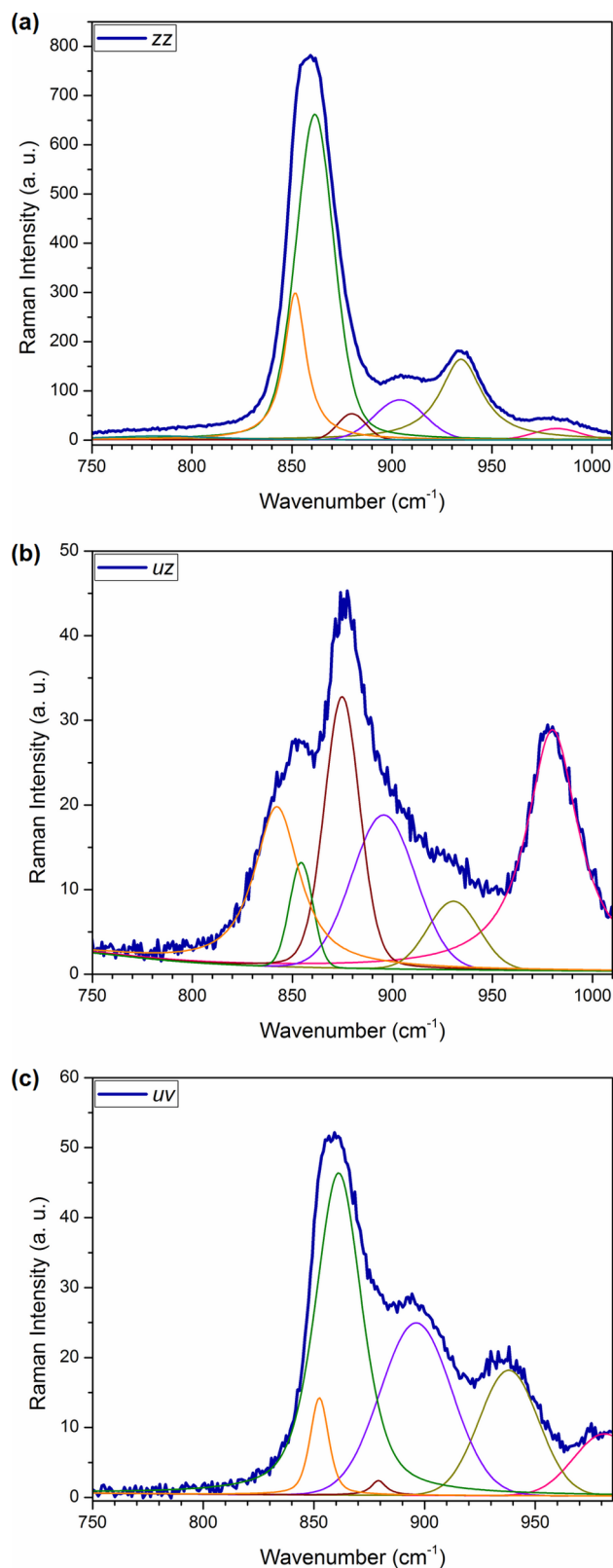
Figure 6. Profile fitting of the (a) *zz*, (b) *uz*, and (c) *uv* spectra of the as-grown $Nd_{9.33}Si_6O_{26}$ single crystal in the region of ν_1 and ν_3 internal modes of SiO_4 tetrahedra.

on the compositions) around the following values: $\nu_1 \sim 850$ cm^{-1}, $\nu_3 \sim 930$ cm^{-1}, $\nu_2 \sim 400$ cm^{-1}, and $\nu_4 \sim 530$ cm^{-1}.[45−49] These internal modes and symmetries are summarized in Tables S3 and S4 of the SI. As the $Nd_{9.33}Si_6O_{26}$ single crystals were grown along the

Table 7. Refined Lattice and Atomic Parameters from Laue Neutron Diffraction in $P6_3/m$ of $Nd_{(28+x)/3}Al_xSi_{6-x}O_{26}$ for x = 0.5, 1.0, and 1.5 at 100 K

x	0.5	1.0	1.5
a (Å)	9.5515	9.553	9.5611
c (Å)	7.042	7.0496	7.0607
volume (Å³)	556.3778	557.1533	558.9772
GOF	1.76	2.17	1.83
R (%)	9.17	6.05	6.39
R_w (%)	4.93	8.63	7.02
Nd(1),4f,($^1/_3$ $^2/_3$ z)			
z	0.0001 (1)	0.00012(9)	0.00021(8)
occupancy	0.913(5)	0.977(5)	0.990(5)
U_{iso} (Å²)	0.0118(3)	0.0111(2)	0.0073(2)
Nd(2),6h,(x y $^1/_4$)			
x	0.00997(8)	0.00944(7)	0.00844(6)
y	0.24121(9)	0.24127(7)	0.24124(6)
U_{iso} (Å²)	0.0074(2)	0.0066(2)	0.0042(2)
Si/Al, 6h, (x y $^1/_4$)			
x	0.4010(2)	0.4014(1)	0.4016(1)
y	0.3719(2)	0.3722(1)	0.3722(1)
U_{iso} (Å²)	0.0073(4)	0.0067(3)	0.0048(3)
O(1), 6h, (x y $^1/_4$)			
x	0.3216(2)	0.3220(1)	0.3222(1)
y	0.4874(2)	0.4888(1)	0.4896(1)
U_{iso} (Å²)	0.0175(4)	0.0151(3)	0.0119(3)
O(2), 6h, (x y $^1/_4$)			
x	0.5988(1)	0.6006(1)	0.6020(1)
y	0.4725(1)	0.4721(1)	0.4719(1)
U_{iso} (Å²)	0.0150(4)	0.0136(3)	0.0101(3)
O(3), 12i, (x y z)			
occupancy	0.806(9)	0.853(7)	0.910(7)
x	0.3514(3)	0.3499(2)	0.3481(2)
y	0.2547(2)	0.2541(1)	0.2533(1)
z	0.0615(2)	0.0614(2)	0.0614(1)
U_{iso} (Å²)	0.0133(5)	0.0123(4)	0.0104(3)
O(3)′, 12i, (x y z)			
occupancy	0.194(9)	0.147(7)	0.090(7)
x	0.3039(12)	0.301(1)	0.297(2)
y	0.2424(8)	0.2397(8)	0.236(1)
z	0.0866(9)	0.0862(9)	0.086(1)
U_{iso} (Å²)	0.0133(5)	0.0123(4)	0.0104(3)
O(4), 2a, (0 0 $^1/_4$)			
U_{iso} (Å²)	0.0250(6)	0.0212(5)	0.0158(4)

Table 8. Refined Anisotropic Atomic Displacement Parameters from Laue Neutron Diffraction in $P6_3/m$ of $Nd_{(28+x)/3}Al_xSi_{6-x}O_{26}$ for x = 0.5, 1.0, and 1.5 at 100 K

x	0.5	1.0	1.5
Nd (1), 4f, (1/32/3z)			
U_{11}	0.0116(4)	0.0132(3)	0.0091(3)
U_{33}	0.0122(4)	0.0071(3)	0.0037(3)
Nd (2), 6h, (x y 1/4)			
U_{11}	0.0066(3)	0.0061(2)	0.0041(2)
U_{22}	0.0069(3)	0.0062(2)	0.0035(2)
U_{33}	0.0070(2)	0.0061(2)	0.0043(2)
U_{12}	0.0022(2)	0.0020(2)	0.0014(2)
Si/Al, 6h, (x y 1/4)			
U_{11}	0.0083(5)	0.0074(4)	0.0048(4)
U_{22}	0.0069(5)	0.0063(4)	0.0045(4)
U_{33}	0.0076(4)	0.0070(3)	0.0055(4)
U_{12}	0.0044(5)	0.0039(3)	0.0026(3)

Table 8. continued

x	0.5	1.0	1.5
O (1), 6h, (x y 1/4)			
U_{11}	0.0252(6)	0.0215(4)	0.0174(4)
U_{22}	0.0197(6)	0.0145(4)	0.0103(3)
U_{33}	0.0151(4)	0.0133(3)	0.0104(3)
U_{12}	0.0170(5)	0.0120(3)	0.0086(3)
O (2), 6h, (x y 1/4)			
U_{11}	0.0107(5)	0.0103(4)	0.0079(3)
U_{22}	0.0093(5)	0.0084(3)	0.0063(3)
U_{33}	0.0222(5)	0.0203(4)	0.0152(3)
U_{12}	0.0028(4)	0.0034(3)	0.0029(3)
O (3), 12i, (x y z)			
U_{11}	0.021(1)	0.0181(7)	0.0153(6)
U_{22}	0.0136(4)	0.0125(3)	0.0097(3)
U_{33}	0.0086(4)	0.0087(3)	0.0077(3)
U_{12}	0.0107(5)	0.0095(4)	0.0073(3)
U_{13}	−0.0041(5)	−0.0044(3)	−0.0046(3)
U_{23}	−0.0024(3)	−0.0020(2)	−0.0015(2)
O (4), 2a, (0 0 1/4)			
U_{11}	0.0136(7)	0.0111(5)	0.0082(4)
U_{33}	0.048(1)	0.042(1)	0.0310(9)

crystallographic c axis,[24] a transverse section coincides with the ab basal plane, and the c direction is contained in a longitudinal

section along the direction of crystal growth. Thus, u and v denote two arbitrary but perpendicular directions within the ab basal plane, and u is perpendicular to the c axis in the longitudinal section (Figure 2). Spectra were measured in backscattering configuration in these two planes, both in parallel and crossed polarizations, i.e., with the scattered electric field either parallel or perpendicular to the incident excitation. Figure 3 shows Raman spectra recorded in the as-grown $Nd_{9.33}Si_6O_{26}$ single crystals in three experimental configurations: zz and uz in a longitudinal section and uv in a transverse section, where the usual notation $\alpha\beta$ is used for incident and scattered electric field polarization along α and β, respectively. These three spectra allow full identification of mode symmetries, giving A_g (zz), E_{1g} (uz), and E_{2g} (uv) modes in $P6_3/m$. It should be noted that the selection rules for A, E_1, and E_2 modes in the case of $P6_3$ space group are the same as for A_g, E_{1g}, and E_{2g} in $P6_3/m$. Spectra were decomposed as a sum of pseudo-Voigt profile bands with the aid of LabSpec software, with position, width, integrated area, and Gaussian/Lorentzian mixing factor of each band used as fitting parameters. Experimental frequencies obtained for the as-grown sample are listed in Table 3. In total, 22 A_g, 21 E_{1g}, and 23 E_{2g} are identified, which is significantly less than the total number of modes of 90 (30 A + 30 E_1 + 30 E_2) in $P6_3$ (with split O(1), O(3) and O(4) sites as determined by neutron diffraction). However, the total number of modes in $P6_3/m$ space group (with split
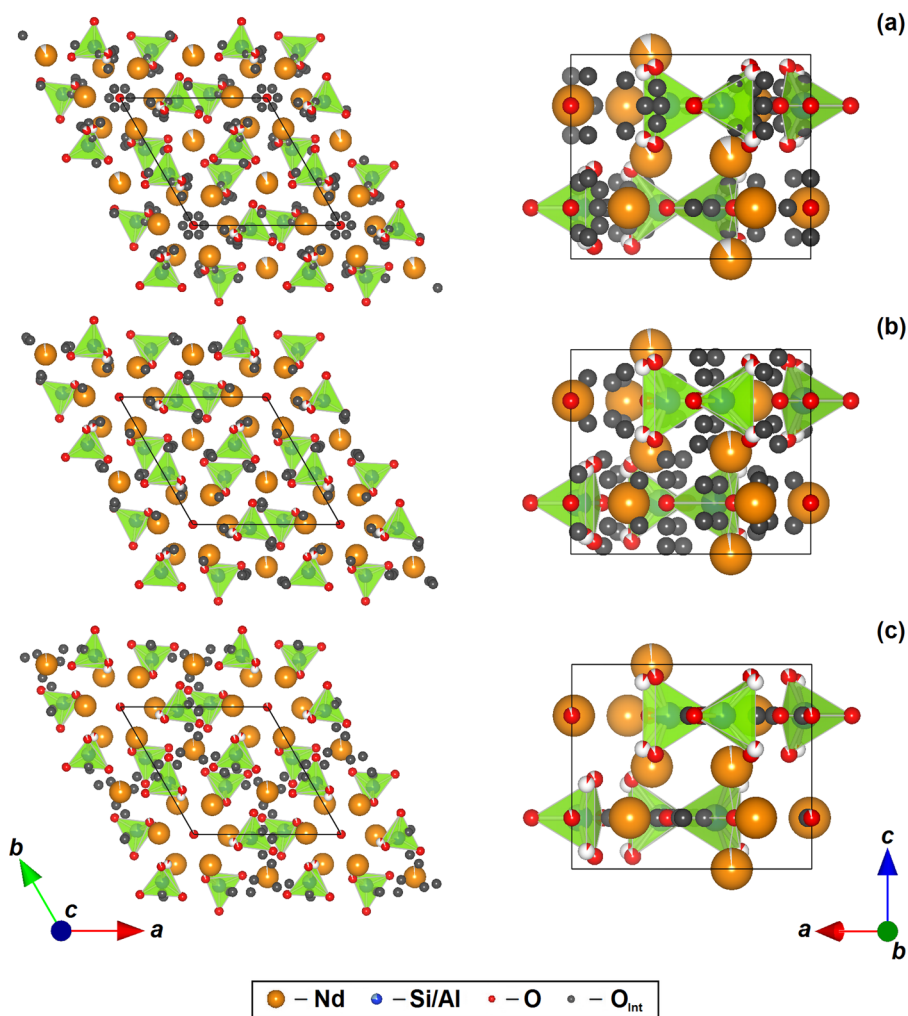

Figure 7. Concentration and distribution of oxygen interstitials at 100 K in $P6_3/m$ $Nd_{(28+x)/3}Al_xSi_{6-x}O_{26}$ with (a) $x = 0.5$, (b) $x = 1.0$, and (c) $x = 1.5$ viewed along [001] (left) and [010] (right). The occupancy of each element is represented by the filled area of the sphere.

Table 9. Oxygen Interstitial Positions and Peak Concentrations from Laue Neutron Diffraction of $P6_3/m$ $Nd_{(28+x)/3}Al_xSi_{6-x}O_{26}$ for $x = 0.5$, 1.0, and 1.5 at 100 K, Arranged from Highest to Lowest Concentration

	x	y	z	conc. (Å^{-3})
$x = 0.5$				
$O_{Int}1$	0.6888	0.0324	0.1431	0.069
$O_{Int}2$	0.8069	0.0350	0.1261	0.065
$O_{Int}3$	0.9272	−0.0014	0.1058	0.064
$O_{Int}4$	0.7760	0.1509	1/4	0.064
$O_{Int}5$	0.8026	0.1129	1/4	0.064
$O_{Int}6$	0.4142	0.5105	1/4	0.062
$O_{Int}7$	0.7600	0.1197	0.1625	0.062
$x = 1.0$				
$O_{Int}1$	0.0700	0.2853	0.1405	0.065
$O_{Int}2$	0.3816	0.5552	0.1616	0.065
$O_{Int}3$	0.8045	0.0307	0.1096	0.060
$O_{Int}4$	0.5319	0.1348	0.0377	0.059
$O_{Int}5$	0.5545	0.1557	0.1357	0.059
$x = 1.5$				
$O_{Int}1$	0.4882	0.0371	1/4	0.055
$O_{Int}2$	0.6129	0.1592	1/4	0.053
$O_{Int}3$	0.4471	0.4636	1/4	0.053
$O_{Int}4$	0.5866	0.2295	1/4	0.053

O(1) and O(3) sites as determined by neutron diffraction) is 51 (18 A_g + 14 E_{1g} + 19 E_{2g}), which is closer to the experimental results and the discrepancy may be attributed to the contribution of oxygen interstitials and local symmetry lowering of perturbed SiO_4 units that are to be discussed in the subsequent section. It should also be noted that O(2) has very anisotropic atomic displacement with a much larger magnitude along the c axis direction (Table 2), and therefore this disorder could also be modeled by a O(2)′ split site, which has $12i$ symmetry and thus contributes additional 9 (3 A_g + 3 E_{1g} + 3 E_{2g}) modes, making the total number of modes to be 60 (21 A_g + 17 E_{1g} + 22 E_{2g}), which is even closer to the experimental results. However, such site splitting is less noticeable than O(1)′ and O(3)′ as it splits along the shorter c axis, and it can also be effectively modeled using anisotropic displacements. (In fact, in order to minimize the number of parameters to improve the data refinement stability, we choose to split only the O(3) site in Table 4.) It can be therefore concluded that $Nd_{9.33}Si_6O_{26}$ is consistent with $P6_3/m$ space group, rather than $P6_3$. Compared to our previous Raman study of $Nd_8Sr_2Si_6O_{26}$,[29] whose experimental results fit very well with $P6_3/m$ without any oxygen split sites, the additional Raman modes in $Nd_{9.33}Si_6O_{26}$ are thus attributed to oxygen site and interstitial disorder introduced by cation vacancies, but not long-range symmetry lowering to $P6_3$.

Neutron diffraction allowed the detection of Frenkel-type defects with oxygen entering interstitial positions along the [001] channel center (O(6) in $P6_3$ and O(5) in $P6_3/m$). Tables 4 and 5 list the atomic positions and displacement parameters of undoped $Nd_{9.33}Si_6O_{26}$ over a range of temperatures from the Laue diffraction data. However, the signals from interstitial positions are weaker than the O(3)′ split sites, and their occupancies could not be successfully refined. Nonetheless, their existence is unequivocal from Fourier mapping (Figure 4) that permits positional specification and provides an estimate of concentration (Table 6). There was little temperature dependence on the abundance of oxygen interstitials from 4K to room

Table 10. Refined Atomic Parameters from Fixed Wavelength Neutron Diffraction of As-Grown and Annealed $P6_3/m$ $Nd_{9.33}Si_6O_{26}$ at Room Temperature

crystal sample	as-grown	annealed
GOF	6.51	5.96
R (%)	5.14	3.99
R_w (%)	7.57	7.20
Nd(1),$4f$,($^1/_3$ $^2/_3$ z)		
z	−0.0011(2)	−0.0011(2)
occupancy	0.889(8)	0.844(7)
U_{iso} (Å^2)	0.0154(5)	0.0136(5)
Nd(2),$6h$,(x y $^1/_4$)		
x	0.0106(1)	0.0113(1)
y	0.2404(1)	0.2423(1)
U_{iso} (Å^2)	0.0093(4)	0.0071(4)
Si, $6h$, (x y $^1/_4$)		
x	0.4009(2)	0.4003(2)
y	0.3719(2)	0.3711(2)
U_{iso} (Å^2)	0.0086(6)	0.0069(5)
O(1), $6h$, (x y $^1/_4$)		
x	0.3228(2)	0.3213(2)
y	0.4872(2)	0.4856(2)
U_{iso} (Å^2)	0.0220(6)	0.0209(6)
O(2), $6h$, (x y $^1/_4$)		
x	0.5967(2)	0.5956(2)
y	0.4735(2)	0.4734(2)
U_{iso} (Å^2)	0.0176(5)	0.0153(5)
O(3), $12i$, (x y z)		
occupancy	0.75(1)	0.72(1)
x	0.3528(5)	0.3536(5)
y	0.2550(2)	0.2545(2)
z	0.0620(3)	0.0612(3)
U_{iso} (Å^2)	0.0155(8)	0.0128(8)
O(3)′, $12i$, (x y z)		
occupancy	0.25(1)	0.28(1)
x	0.304(1)	0.307(1)
y	0.2442(8)	0.2438(7)
z	0.086(1)	0.0846(9)
U_{iso} (Å^2)	0.0155(8)	0.0128(8)
O(4), $2a$, (0 0 $^1/_4$)		
occupancy	0.96(2)	1.04(1)
U_{iso} (Å^2)	0.031(1)	0.0225(8)

temperature, but from 300 to 773 K the number of detected sites varied from 4 to 9, with the highest number found for 773 K (Figure 5). The interstitial positions also vary with temperature, and while the interstitial oxygen resident in the tunnel is very close (0.001−0.003 Å) to the c axis from 4−300 K, it becomes displaced from the channel center at elevated temperatures (0.69 Å at 573 K and 0.54 Å at 773 K). In addition, new interstitial sites appear in the tunnel at 573 K and between the SiO_4 tetrahedra at 773 K.

It should be noted that these oxygen interstitials could also contribute additional Raman modes. Table S5 in the SI summarizes Raman activity that oxygen interstitials may contribute, based on their positions and symmetries. The interplay between cation vacancies, oxygen sublattice distortion and Raman spectra can be better elucidated by careful study of $[SiO_4]$ internal modes, which are expected to be very sensitive to split oxygen sites and Si—O distances. The region of stretching modes (>800 cm^{-1}) is especially informative due to the absence of overlapping lattice modes. Figure 6 shows the decomposition

Table 11. Refined Anisotropic Atomic Displacement Parameters from Fixed Wavelength Neutron Diffraction of As-Grown and Annealed $P6_3/m$ $Nd_{9.33}Si_6O_{26}$ at Room Temperature

crystal sample	as-grown	annealed
Nd (1), 4f, (1/32/3 z)		
U_{11}	0.0118(6)	0.0083(5)
U_{33}	0.0226(9)	0.0243(9)
Nd (2), 6h, (x y 1/4)		
U_{11}	0.0082(5)	0.0065(5)
U_{22}	0.0105(5)	0.0069(5)
U_{33}	0.0076(6)	0.0070(5)
U_{12}	0.0033(3)	0.0026(3)
Si/Al, 6h, (x y 1/4)		
U_{11}	0.0105(8)	0.0073(7)
U_{22}	0.0097(7)	0.0073(7)
U_{33}	0.0060(7)	0.0063(7)
U_{12}	0.0055(6)	0.0038(6)
O (1), 6h, (x y 1/4)		
U_{11}	0.0339(8)	0.0309(8)
U_{22}	0.0300(8)	0.0292(8)
U_{33}	0.0163(7)	0.0170(7)
U_{12}	0.0267(7)	0.0259(7)
O (2), 6h, (x y 1/4)		
U_{11}	0.0127(7)	0.0099(6)
U_{22}	0.0128(6)	0.0101(6)
U_{33}	0.0232(8)	0.0212(7)
U_{12}	0.0033(5)	0.0014(4)
O (3), 12i, (x y z)		
U_{11}	0.025(1)	0.020(2)
U_{22}	0.0165(6)	0.0132(6)
U_{33}	0.0084(8)	0.0072(8)
U_{12}	0.0130(8)	0.0095(8)
U_{13}	−0.0054(8)	−0.0034(8)
U_{23}	−0.0040(4)	−0.0030(4)
O (4), 2a, (0 0 1/4)		
U_{11}	0.015(1)	0.0138(9)
U_{33}	0.062(2)	0.040(2)

of zz (A_g), uz (E_{1g}), and uv (E_{2g}) spectra for the as-grown $Nd_{9.33}Si_6O_{26}$ in this region, from which 6 A_g, 6 E_{1g}, and 6 E_{2g} bands are identified, which are clearly more than expected from ν_1 and ν_3 bands altogether (Table S4). This discrepancy is due to the fact that in Table S4, only one single type of SiO_4 tetrahedra is assumed in which all Si environments are identical and each SiO_4 group consists of only four oxide ions. In reality, the splitting of oxygen sites leads to (at least) two types of SiO_4 tetrahedra, either perturbed or unperturbed by the presence of adjacent Nd vacancies. The multiplication of internal modes due to the existence of different types of SiO_4 tetrahedra is clearly manifested in the high frequency zz spectrum (Figure 6(a)), whose ν_1 band consists of two main components at ~852 and ~861 cm^{-1} and a third, weaker one at ~880 cm^{-1}. The appearance of two A_g breathing modes is not compatible with the expectations for a single type of tetrahedra (Table S4) and requires the assumption of multiple environments for Si. In fact, symmetry lowering to $P6_3$ also fails to explain this result, as it also predicts only one A mode in the ν_1 region (Table S3). If the two main components of ν_1 are due to two distinct tetrahedra, namely those perturbed or unperturbed by adjacent vacancies, then the intensities can be compared with predictions of vacancy concentration. The intensities depend on the fitting parameters,

with representative values being $I(854)/Sum = 0.3 \pm 0.07$. Here, the low frequency components are assigned to the unperturbed tetrahedra and high frequency ones to the perturbed tetrahedra, in accord with Guillot et al.,[45] who stated that a vacancy at the Nd(1) site would push the neighboring oxygen atoms away, thus shortening the Si—O bonds and resulting in frequency increase for the breathing mode. Our attribution is also in agreement with the observations made by Wu et al. in $RE_{9.33}(SiO_4)_6O_2$ apatites where the splitting of the ν_1 mode was seen to increase with decreasing ionic radius of the rare earth cation.[49] Within this hypothesis, the ratio between the Raman intensities fits rather well with the populations of unperturbed and perturbed tetrahedra as derived from the concentration of Nd(1) vacancies and the number of neighboring tetrahedra (six), which yield a theoretical ratio of 1/3 to 2/3 between them.

However, while the assumption of two types of SiO_4 tetrahedra explains the results for A_g and E_{2g} symmetries, a clear discrepancy remains in the number of E_{1g} modes. In particular, no E_{1g} mode is expected in the ν_1 region and only two in the ν_3 region, which is far from the six experimentally observed in uz geometry. This can be attributed to a local symmetry lowering of the perturbed SiO4 units from C_s to C_1 when split oxygen sites are considered in the Si environment with $O(1)'$ and $O(2)'$ out of the mirror plane. As shown in Table S6, symmetry lowering to C_1 for SiO_4 yields split ν_1 as $A_g + E_{1g} + E_{2g}$, consistent with the detection of an E_{1g} mode in the ν_1 region, as well as extra E_{1g} modes in the ν_3 region.

Interpretation is less clear for ν_2 and ν_4 bands, due to the overlap of other modes (mainly channel and interstitial oxygen vibration). In total, 3 A_g, 4 E_{1g}, and 5 E_{2g} are identified in the ν_2 region around 400 cm^{-1} and 4 A_g, 4 E_{1g}, and 4 E_{2g} in the ν_4 region of 530 cm^{-1}, which could also be attributed to oxygen site splitting and lower local symmetry.

The lattice and atomic parameters of Al-doped $Nd_{(28+x)/3}Al_x$-$Si_{6-x}O_{26}$ ($x = 0.5, 1.0$, and 1.5) are listed in Tables 7 and 8. As Al^{3+} ($IR = 0.39$ Å)[50] is larger than Si^{4+} (0.26 Å),[50] both a and c increase as the crystals become more aluminous. For the dilated unit cell, steric hindrance toward oxygen migration is reduced. The O(3) order was also improved, reflected in less occupancy at the $O(3)'$ split site as x increases. Figure 7 shows the distribution of the interstitial sites at 100 K for $Nd_{(28+x)/3}Al_xSi_{6-x}O_{26}$ ($x = 0.5, 1.0$, and 1.5), with their locations and concentrations listed in Table 9. As the crystals become more aluminous, the abundance of interstitials is reduced ($2Si^{4+} + O_i^{2-} \rightarrow 2Al^{3+} + \square_i$) and the interstitials originating in the tunnel move toward the framework, while simultaneously the Nd^F vacancy concentration decreases ($\square_{Nd} + 3Si^{4+} \rightarrow Nd^{3+} + 3Al^{3+}$). At $x = 1.5$, the tunnel is devoid of interstitials, which are then located in the framework.

To better correlate crystal chemistry with functionality, samples with poorer conductivity were also examined. Tables 10 and 11 list the atomic positions and displacement parameters of the undoped $Nd_{9.33}Si_6O_{26}$ that has been annealed for 3 months at 950 °C as compared with the as-grown crystal. For better calculation and display of interstitial positions, splitting of oxygen sites other than $O(3)'$ are not included during data fitting, resulting in a poorer GOF for the undoped $Nd_{9.33}Si_6O_{26}$ to the $P6_3/m$ model at room temperature. Overall, the annealed crystal is better ordered, as O(4) is fully occupied and the Nd(1) occupancy is closer to the ideal value (0.833) per formula unit. The interstitial positions and concentrations at Fourier peaks of $Nd_{9.33}Si_6O_{26}$ (prior to and after annealing) are illustrated in Figure 8 and collated in Table 12. In an analogous fashion to Al-doping, the tunnel interstitials in $Nd_{9.33}Si_6O_{26}$ migrate toward
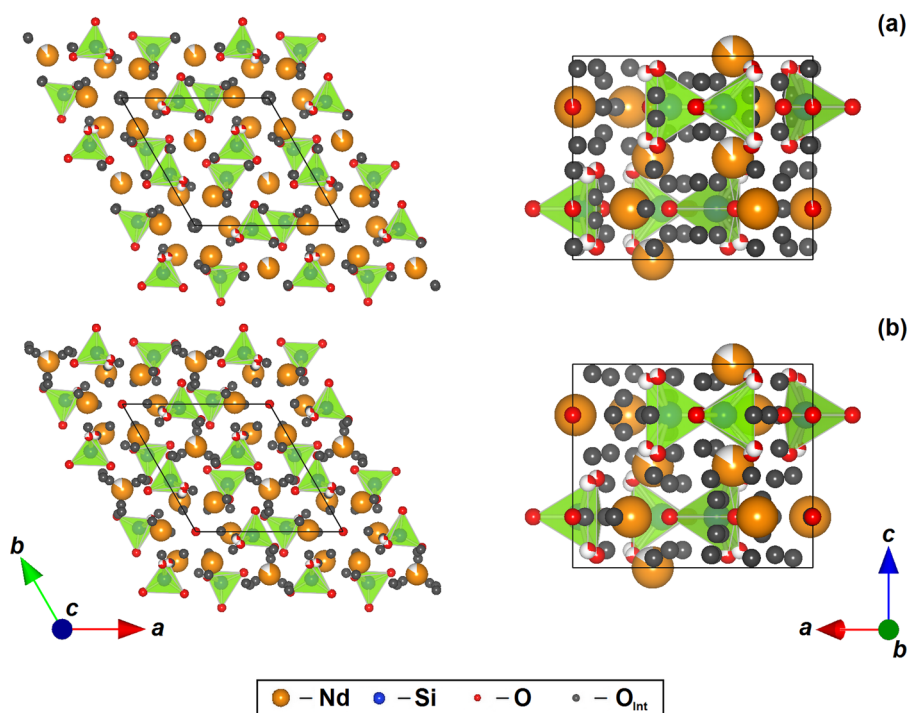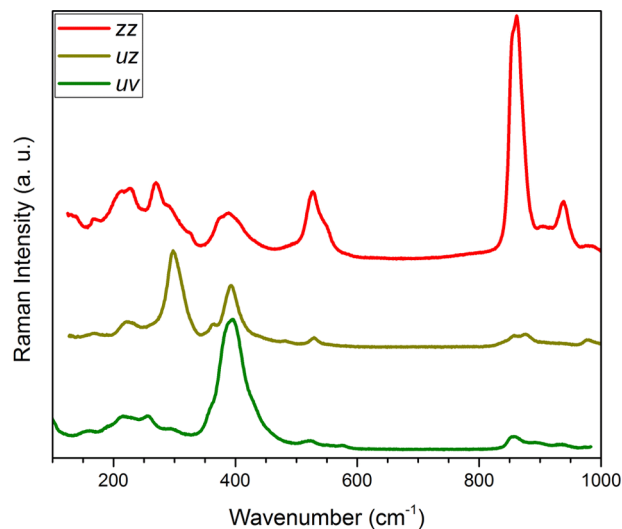
Figure 8. Concentration and distribution of oxygen interstitials in (a) as-grown $Nd_{9.33}Si_6O_{26}$ and (b) annealed $Nd_{9.33}Si_6O_{26}$ at room temperature viewed along [001] (left) and [010] (right).

Table 12. Oxygen Interstitial Positions and Peak Concentrations from Fixed Wavelength Neutron Diffraction of As-Grown and Annealed $P6_3/m$ $Nd_{9.33}Si_6O_{26}$ at Room Temperature, Arranged from Highest to Lowest Concentration

	x	y	z	conc. ($Å^{-3}$)
as-grown				
$O_{Int}1$	0.9844	0.0042	0.0618	0.10
$O_{Int}2$	0.1003	0.3392	0.0574	0.081
$O_{Int}3$	0.7409	0.0887	0.1930	0.074
$O_{Int}4$	0.6952	0.8210	1/4	0.064
$O_{Int}5$	0.5358	0.1373	0.1276	0.060
$O_{Int}6$	0.3958	0.5243	0.1206	0.060
annealed				
$O_{Int}1$	0.7527	0.0505	1/4	0.055
$O_{Int}2$	0.8184	0.1413	1/4	0.050
$O_{Int}3$	0.0819	0.3374	0.0478	0.045
$O_{Int}4$	0.3858	0.5979	0.1666	0.040
$O_{Int}5$	0.5423	0.1386	0.0868	0.036
$O_{Int}6$	0.4169	0.5739	0.0634	0.036
$O_{Int}7$	0.1688	0.1724	1/4	0.033

Figure 9. Raman spectra of the annealed $Nd_{9.33}Si_6O_{26}$ single crystal.

the framework after annealing, but the overall concentration of interstitials is significantly lower. This may be due to the presence of Si_2O_7 dimers in the framework[51] and the subsequent elimination of interstitials ($O_i^{2-} + Si_2O_7^{6-} \rightarrow 2SiO_4^{4-}$) after heat treatment.

Figure 9 shows the Raman spectra of the annealed $Nd_{9.33}Si_6O_{26}$ crystal (950 °C/3 months) in zz, uz and uv configurations. Raman shifts obtained by profile decomposition are listed in Table 13. While the spectra look similar to those of as-grown samples, there are small but significant differences in the high frequency region, specifically in the relative proportion of the bands composing the breathing ν_1 mode with A_g symmetry. Profile fitting (Figure 10) yields clearly three

components at frequencies close to those of the as-grown crystal but with smaller line widths and different relative intensities. The third component, in particular, is considerably enhanced at the expense of the second one. The ratio between the area of the first component and the integrated area of the whole ν_1 band is, however, quite similar to that found for the as-grown sample with a slight decrease. It should be noted that while fitting spectra with overlapping bands is subject to large errors, such an increase in the third band is beyond fitting errors and thus associated with structural features instead. Since the major difference between these two samples is the shift of the oxygen interstitials in the annealed sample from the channel axis toward a peripheral $6h$ site close to SiO_4 tetrahedra, it is suggested that the third band arises from tetrahedra perturbed by peripheral O_{int}. These ions are not close enough to Si so as to yield a SiO_5 entity, but may have an

Table 13. Raman Shifts (cm^{-1}) of Annealed $Nd_{9.33}Si_6O_{26}$ Crystal Derived from Profile Fitting of *zz*, *uz*, and *uv* Spectra, Yielding A_g, E_{1g}, and E_{2g} Modes, Respectively
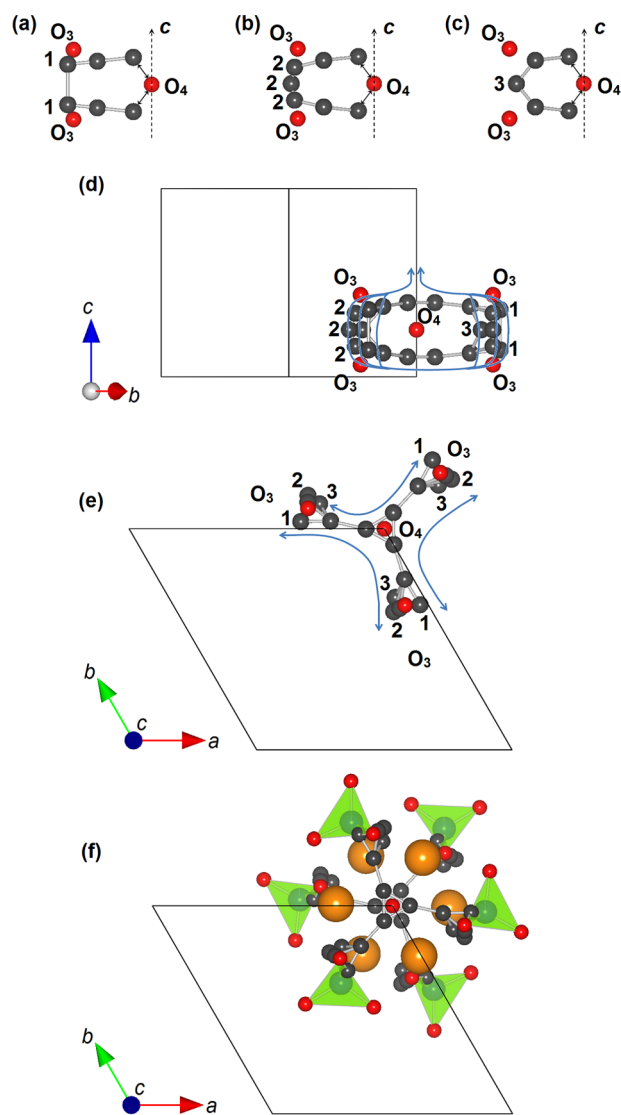
	A_g modes	E_{1g} modes	E_{2g} modes
	132.1	167.6	159.5
	168.7	187.2	190.5
	209.9	217.6	211.1
	230.7	233.2	232.7
	270.0	263.8	259.1
	291.7	295.0	292.6
	308.5	304.7	325.0
	326.9	348.6	361.6
	372.6	361.8	383.3
	391.8	391.5	401.0
	433.4 vb	413.7	431.6
	514.5 vb	438.7	448.8 b
	526.7	481.5	527.0
	547.1	527.8	555.7
	574.4 wb	533.1	579.9
	853.0	837.6	853.5
	862.8	855.1	862.4
	873.6	873.1	886.7 b
	903.0	902.1	935.3
	915.2	932.7	975.1
	938.2	976.0	990.2
	984.2	989.8	
total:	**22**	**22**	**21**
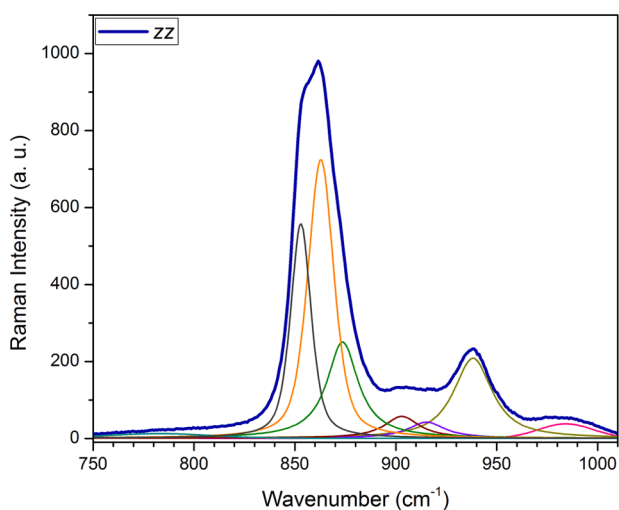
Figure 10. Profile fitting of the *zz* spectrum of the annealed $Nd_{9.33}Si_6O_{26}$ single crystal in the region of ν_1 and ν_3 internal modes of SiO_4 tetrahedra.

Figure 11. O^{2-} conduction paths around the tunnel centered at $(00z)$ deduced from neutron diffraction, which become effective at intermediate SOFC operating temperature (500−700 °C). Oxygen may migrate horizontally between O(4) and O(3) through the interstitial sites (gray color), and vertically between O(3) atoms through 3 possible interstitial paths ((a)−(c)). O^{2-} may thus (d) move along [001] or (e) diffuse in (001) across the tunnel via these transport routes. (f) Per unit cell, there are six SiO_4 tetrahedra, and each has dual-conduction path connected to the tunnel.

effect on oxygen bonding by pushing O3 ions to split $O(3)'$ sites with shorter Si—O bond distances (and thus higher frequencies). This is supported by a slight increase of the significant figures of $O(3)'$ in the annealed sample as compared to the as-grown one (Table 10).

It should also be noted that the discrepancy in the number of E_{1g} modes at high frequency remains in the annealed crystal, which supports our interpretation that it has an intrinsic origin, such as the local symmetry lowering of the SiO_4 unit due to split oxygen sites around cation vacancies. At lower frequencies, differences are suggested to be due to the disappearance of O_{int} in the channel axis and its shift to a new site in the periphery. Specifically, as Table 13 shows, one band of each symmetry type

should disappear, but no clear evidence is found of any modes disappearing in the annealed crystal that might be attributed to the O_{int} at the 4e site. This may be due to several causes: (i) it is possible that those O_{int}, though at the 4e site on average, are in fact highly disordered along the c axis, which may broaden the bands and make them indistinguishable from the background; (ii) these O_{int} are so close to the origin at room temperature that they can be better described as occupying the 2b site (000), which has inversion symmetry and is thus not Raman active (Table S5). However, new bands should be observed in the annealed sample arising from the interstitial oxide ions at the channel periphery. The enhancement of bands at ~290 and ~330 cm^{-1} in *zz* and at ~260 and ~350 cm^{-1} in *uz* could be assigned to these interstitial oxygen atoms, although their symmetries do not fully agree with expectations from an extra 6h site.
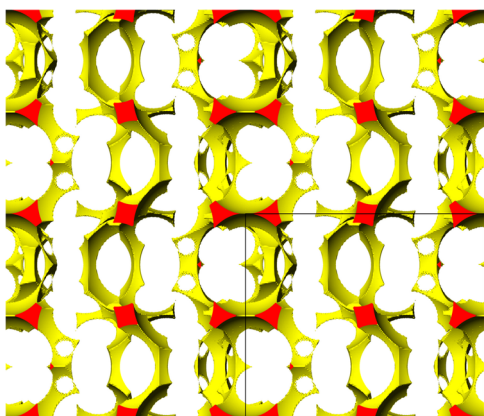
Figure 12. Atomic void space (viewed along [010]) as calculated from Laue diffraction solution of $Nd_{9.33}Si_6O_{26}$ collected at 4 K where the oxygen interstitials are excluded. This representation emphasizes the possible locations of extra-stoichiometric oxygen and the migration path of O^{2-}.

◼ DISCUSSION

Computational approaches suggest two conduction pathways for interstitial oxygen: (i) directly along the c axis tunnel center, with O^{2-} progressing through adjacent interstitial sites including the residence at the O(4) position;[9,16] or (ii) across the ab basal plane, where mobility is facilitated by the presence of Nd^F framework interstitials,[14,18] or realized through tilting of SiO_4 tetrahedra.[15] Here, the first direct observation of interstitial O^{2-} is consistent with transportation pathways involving O(4) and two O(3) (Figure 11). The interstitials enable horizontal (ab plane) conduction from O(3) to the tunnel O(4) locations together with vertical routes (c axis) between the two O(3) of the SiO_4 tetrahedron. In combination, these mechanisms show that oxygen migration is best considered as a whole-of-crystal percolation. The interstitial positions confirm two alternate migration paths along the tunnel, and facilitate conduction between the SiO_4 tetrahedra through the tunnel walls in a manner similar to $La_{9.69}Si_{5.70}$-$Mg_{0.30}O_{26.24}$.[52] The Laue diffraction data of undoped $Nd_{9.33}Si_6O_{26}$ collected at 4 K reveal the void space within the lattice (Figure 12), through which migration of oxygen takes places along [001].

If undoped $Nd_{9.33}Si_6O_{26}$ is heated toward the SOFC operating temperature (500−700 °C), then the putative $4e$ interstitials shift to locations near the c axis with $12i$ symmetry (Figure 5), and ionic conductivity is steadily enhanced as interstitial concentration increases. At 573 K, more interstitial sites become available within the tunnel and a dual-conduction path is created at 773 K. This boosts conductivity and correlates with the inflection evident in the [001] $\log(\sigma T)$ against $1/T$ plots.[53] This feature is, however, absent after annealing as the c-axis interstitials move away from the tunnel, the split conduction routes cannot form, and conductivity is lowered.

For Al-doped $Nd_{(28+x)/3}Al_xSi_{6-x}O_{26}$, the tunnel interstitials also move further into the framework as x increases (Figure 7). With the dual-conduction path removed, the ionic conductivity along c axis decreases as the crystal becomes more aluminous. However, as the interstitials enter the framework, the oxygen mobility across the ab basal plane is enhanced. Also, without increased tunnel interstitials at elevated temperature, no inflection has been observed in the conductivity plots of these Al-doped crystals.[25]

◼ CONCLUSIONS

Neutron diffraction with Laue and fixed wavelength four-circle methods was performed on single crystals of $Nd_{(28+x)/3}Al_xSi_{6-x}O_{26}$

($x = 0$, 0.5, 1.0, and 1.5) and provided comparable structure solutions. All Laue diffraction data fitted $P6_3/m$. Compared with single crystal X-ray diffraction of Al-doped apatites,[25] Laue diffraction yielded an improved GOF when the O(3) site is split and better definition of the large cation displacement parameters. While treatment of Laue diffraction data of undoped $Nd_{9.33}Si_6O_{26}$ collected at 2 K shows a slightly better GOF with $P6_3$, primarily due to better fitting of Nd^F vacancy distribution, the evidence is not sufficiently compelling to discard the $P6_3/m$ model (at least for the materials used). A separate study with Raman spectroscopy also confirmed the as-grown $Nd_{9.33}Si_6O_{26}$ crystal to have $P6_3/m$ symmetry. Raman work also confirmed the split of oxygen sites, though O(1)′ and O(2)′ can also be modeled by large anisotropic atomic displacements.

The direct observation of oxygen interstitials shows for the first time the different modalities connecting the tunnel O(4) to the framework SiO_4 tetrahedra via O(3) atoms, that facilitates ionic conduction in two principal directions.

(i) For O^{2-} migration along [001], this conduction path can serve as an alternate route, in addition to those deduced from computational studies.[9,16,18] For undoped $Nd_{9.33}Si_6O_{26}$, it was also found that additional tunnel interstitials become available at 573−773 K, which enhances the O^{2-} transport and results in the distinctive inflection in the conductivity plot against temperature. This structural change takes place at intermediate temperatures, and should prove beneficial when oxyapatites are deployed in SOFC.

(ii) For O^{2-} transport perpendicular to [001], intertunnel conduction provides an auxiliary diffusion pathway within the framework structure realized by lattice cavities (revealed by this work), interstitials,[18] and probably exchange processes involving the formation of transitory Si_2O_9 dimers.[15] Such exchange processes are supported by the observation from ^{17}O NMR studies of the ready exchange of the oxide ions of the Si/GeO_4 groups.[23,54]

The tunnel interstitials shift toward the framework when the crystal is doped with Al or subjected to long-term annealing. With the dual-conduction path disabled, O^{2-} migration along the c axis is attenuated, and very well described by previously published mechanisms derived from simulation. This change is reflected in the removal of the inflection in the conductivity plot. However, for the Al-doped series $Nd_{(28+x)/3}Al_xSi_{6-x}O_{26}$, the ionic conductivity across the ab basal plane increases as these interstitials move into the framework. This is consistent with earlier magic angle spinning nuclear magnetic resonance (MAS NMR) studies,[47,55] that showed that stoichiometric $La_8Sr_2Si_6O_{26}$ displayed a single resonance corresponding to the SiO_4 group, while in $La_9SrSi_6O_{26.5}$ containing excess oxygen, an additional resonance associated with interstitial oxygen adjacent to SiO_4 (i.e., SiO_5) was observed. This experimental determination of interstitial distribution and the discovery of the dual-conduction path at intermediate temperatures provide a systematic understanding of oxide migration in oxyapatites, and these insights can guide future performance optimization.

◼ ASSOCIATED CONTENT

Ⓢ Supporting Information

The Supporting Information is available free of charge on the ACS Publications website at DOI: 10.1021/jacs.5b13409.

Raman active modes; (Table S1) Raman activity in $P6_3$ space group; (Table S2) Raman activity in $P6_3/m$ space

group; (Table S3) internal modes of SiO$_4$ in P6$_3$ space group; (Table S4) internal modes of SiO$_4$ in P6$_3$/m space group; (Table S5) Raman activity of possible oxygen interstitials in P6$_3$/m space group; and (Table S6) internal modes of perturbed SiO$_4$ in P6$_3$/m space group (PDF)
Single crystal neutron diffraction data in Crystallographic Information File (CIF) format, Raman activities and internal modes of different space symmetries, oxygen interstitials and perturbed SiO$_4$ tetrahedra (CIF)

(TXT)
(CIF)
(TXT)
(CIF)
(TXT)
(CIF)
(TXT)
(CIF)
(TXT)
(CIF)
(TXT)
(CIF)
(TXT)

■ AUTHOR INFORMATION

Corresponding Authors
*jwei@simtech.a-star.edu.sg
*tjwhite@ntu.edu.sg

Present Address
▼Institute of Materials Research and Engineering (IMRE), Agency for Science, Technology and Research (A*STAR), 2 Fusionopolis Way, Innovis, #08−03, Singapore 138634, Singapore.

Notes
The authors declare no competing financial interest.

■ REFERENCES

(1) Stambouli, A. B.; Traversa, E. *Renewable Sustainable Energy Rev.* **2002**, *6*, 433.
(2) Minh, N. Q. *J. Am. Ceram. Soc.* **1993**, *76*, 563.
(3) Carrette, L.; Friedrich, K. A.; Stimming, U. *Fuel Cells* **2001**, *1*, 5.
(4) Ishihara, T.; Sammes, N. M.; Yamamoto, O. In *High Temperature Solid Oxide Fuel Cells: Fundamentals, Design and Applications*; Singhal, S., Kendall, K., Eds.; Elsevier: Oxford, 2003; p 83.
(5) Nakayama, S.; Sakamoto, M. *J. Eur. Ceram. Soc.* **1998**, *18*, 1413.
(6) Baikie, T.; Ng, M. H. G.; Madhavi, S.; Pramana, S. S.; Blake, K.; Elcombe, M.; White, T. J. *Dalton Trans.* **2009**, 6722.
(7) Pramana, S. S.; Klooster, W. T.; White, T. J. *J. Solid State Chem.* **2008**, *181*, 1717.
(8) Masubuchi, Y.; Higuchi, M.; Takeda, T.; Kikkawa, S. *Solid State Ionics* **2006**, *177*, 263.
(9) Tolchard, J. R.; Islam, M. S.; Slater, P. R. *J. Mater. Chem.* **2003**, *13*, 1956.
(10) Kendrick, E.; Islam, M. S.; Slater, P. R. *J. Mater. Chem.* **2007**, *17*, 3104.
(11) Abram, E. J.; Sinclair, D. C.; West, A. R. *J. Mater. Chem.* **2001**, *11*, 1978.
(12) Slater, P. R.; Sansom, J. E. H.; Tolchard, J. R. *Chem. Rec.* **2004**, *4*, 373.
(13) Arikawa, H.; Nishiguchi, H.; Ishihara, T.; Takita, Y. *Solid State Ionics* **2000**, *136−137*, 31.
(14) Pramana, S. S.; Klooster, W. T.; White, T. J. *Acta Crystallogr., Sect. B: Struct. Sci.* **2007**, *63*, 597.
(15) Jones, A.; Slater, P. R.; Islam, M. S. *Chem. Mater.* **2008**, *20*, 5055.
(16) Béchade, E.; Masson, O.; Iwata, T.; Julien, I.; Fukuda, K.; Thomas, P.; Champion, E. *Chem. Mater.* **2009**, *21*, 2508.
(17) Liao, T.; Sasaki, T.; Suehara, S.; Sun, Z. *J. Mater. Chem.* **2011**, *21*, 3234.
(18) Matsunaga, K.; Toyoura, K. *J. Mater. Chem.* **2012**, *22*, 7265.
(19) Guillot, S.; Beaudet-Savignat, S.; Lambert, S.; Vannier, R.-N.; Roussel, P.; Porcher, F. *J. Solid State Chem.* **2009**, *182*, 3358.
(20) Liao, T.; Sasaki, T.; Sun, Z. *Phys. Chem. Chem. Phys.* **2013**, *15*, 17553.
(21) Fukuda, K.; Asaka, T.; Okino, M.; Berghout, A.; Béchade, E.; Masson, O.; Julien, I.; Thomas, P. *Solid State Ionics* **2012**, *217*, 40.
(22) Nakayama, S.; Higuchi, M. *J. Mater. Sci. Lett.* **2001**, *20*, 913.
(23) Panchmatia, P. M.; Orera, A.; Rees, G. J.; Smith, M. E.; Hanna, J. V.; Slater, P. R.; Islam, M. S. *Angew. Chem., Int. Ed.* **2011**, *50*, 9328.
(24) An, T.; Baikie, T.; Wei, F.; Li, H.; Brink, F.; Wei, J.; Ngoh, S. L.; White, T. J.; Kloc, C. *J. Cryst. Growth* **2011**, *333*, 70.
(25) An, T.; Baikie, T.; Wei, F.; Pramana, S. S.; Schreyer, M. K.; Piltz, R. O.; Shin, J. F.; Wei, J.; Slater, P. R.; White, T. J. *Chem. Mater.* **2013**, *25*, 1109.
(26) Okudera, H.; Yoshiasa, A.; Masubuchi, Y.; Higuchi, M.; Kikkawa, S. *Z. Kristallogr. - Cryst. Mater.* **2004**, *219*, 27.
(27) An, T.; Baikie, T.; Herrin, J.; Brink, F.; Shin, J. F.; Slater, P. R.; Li, S.; White, T. J. *J. Am. Ceram. Soc.* **2013**, *96*, 3457.
(28) McPherson, A. In *Introduction to Macromolecular Crystallography*; John Wiley & Sons, Inc.: New York, 2008; p 211.
(29) An, T.; Orera, A.; Baikie, T.; Herrin, J. S.; Piltz, R. O.; Slater, P. R.; White, T. J.; Sanjuán, M. L. *Inorg. Chem.* **2014**, *53*, 9416.
(30) Campbell, J. W. *J. Appl. Crystallogr.* **1995**, *28*, 228.
(31) Campbell, J. W.; Hao, Q.; Harding, M. M.; Nguti, N. D.; Wilkinson, C. *J. Appl. Crystallogr.* **1998**, *31*, 496.
(32) Wilkinson, C.; Khamis, H. W.; Stansfield, R. F. D.; McIntyre, G. J. *J. Appl. Crystallogr.* **1988**, *21*, 471.
(33) Prince, E.; Wilkinson, C.; McIntyre, G. J. *J. Appl. Crystallogr.* **1997**, *30*, 133.
(34) Campbell, J. W.; Habash, J.; Helliwell, J. R.; Moffat, K. *Inform. Q. Protein Crystallogr.* **1986**, *18*, 23.
(35) Petricek, V.; Dusek, M.; Palatinus, L. *Jana: Crystallographic Computing System*; Institute of Physics: Praha, Czech Republic, 2006.
(36) Momma, K.; Izumi, F. *J. Appl. Crystallogr.* **2008**, *41*, 653.
(37) Scherf, C.; *Institut für Kristallographie ed.*; RWTH Aachen: Aachen, Germany, 1998, Program for data reduction of DIF4.
(38) McIntyre, G.; Institut Laue-Langevin: Grenoble, France, 1983, Program for calculating absorption.
(39) Meven, M.; Hutanu, V.; Heger, G. *Neutron News* **2007**, *18*, 19.
(40) Meven, M.; Sazonov, A. *J. Large-Scale Res. Facil.* **2015**, *1*, A7.
(41) Hutanu, V.; Meven, M.; Heger, G. *Phys. B* **2007**, *397*, 135.
(42) Lonsdale, K. *Mineral. Mag.* **1947**, *28*, 14.
(43) Lambert, S.; Vincent, A.; Bruneton, E.; Beaudet-Savignat, S.; Guillet, F.; Minot, B.; Bouree, F. *J. Solid State Chem.* **2006**, *179*, 2602.
(44) Nakamoto, K. *Infrared and Raman Spectra of Inorganic and Coordination Compounds: Part A: Theory and Applications in Inorganic Chemistry*, 6th ed.; John Wiley & Sons, Inc.: Hoboken, 2009.
(45) Guillot, S.; Beaudet-Savignat, S.; Lambert, S.; Roussel, P.; Tricot, G.; Vannier, R.-N.; Rubbens, A. *J. Raman Spectrosc.* **2011**, *42*, 1455.
(46) Lucazeau, G.; Sergent, N.; Pagnier, T.; Shaula, A.; Kharton, V.; Marques, F. M. B. *J. Raman Spectrosc.* **2007**, *38*, 21.

(47) Orera, A.; Kendrick, E.; Apperley, D. C.; Orera, V. M.; Slater, P. R. *Dalton Trans.* **2008**, 5296.

(48) Smirnov, M.; Sukhomlinov, S.; Mirgorodsky, A.; Masson, O.; Béchade, E.; Colas, M.; Merle-Méjean, T.; Julien, I.; Thomas, P. *J. Raman Spectrosc.* **2010**, *41*, 1700.

(49) Wu, R.; Pan, W.; Ren, X.; Wan, C.; Qu, Z.; Du, A. *Acta Mater.* **2012**, *60*, 5536.

(50) Shannon, R. D. *Acta Crystallogr., Sect. A: Cryst. Phys., Diffr., Theor. Gen. Crystallogr.* **1976**, *32*, 751.

(51) Baikie, T.; Pramana, S. S.; Ferraris, C.; Huang, Y.; Kendrick, E.; Knight; Kevin, S.; Ahmad, Z.; White, T. J. *Acta Crystallogr., Sect. B: Struct. Sci.* **2010**, *66*, 1.

(52) Ali, R.; Yashima, M.; Matsushita, Y.; Yoshioka, H.; Ohoyama, K.; Izumi, F. *Chem. Mater.* **2008**, *20*, 5203.

(53) An, T.; Baikie, T.; Weyland, M.; Shin, J. F.; Slater, P. R.; Wei, J.; White, T. J. *Chem. Mater.* **2015**, *27*, 1217.

(54) Kiyono, H.; Matsuda, Y.; Shimada, T.; Ando, M.; Oikawa, I.; Maekawa, H.; Nakayama, S.; Ohki, S.; Tansho, M.; Shimizu, T.; Florian, P.; Massiot, D. *Solid State Ionics* **2012**, *228*, 64.

(55) Sansom, J. E. H.; Tolchard, J. R.; Islam, M. S.; Apperley, D.; Slater, P. R. *J. Mater. Chem.* **2006**, *16*, 1410.